Using Adhesive Micropatterns and AFM to Assess Cancer Cell Morphology and Mechanics

Maxime Liboz, Antoine Allard, Michel Malo, Guillaume Lamour, Gaelle Letort, Bénédicte Thiébot, Sid Labdi, Juan Pelta, Clément Campillo

Using adhesive micropatterns and AFM to assess cancer cell morphology and mechanics

Maxime Liboz[a], Antoine Allard[a,b], Michel Malo[a], Guillaume Lamour[a], Gaelle Letort[c], Bénédicte Thiébot[d], Sid Labdi[a], Juan Pelta[a], and Clément Campillo[a,e,*]

[a] LAMBE, Univ Evry, CNRS, CEA, Université Paris-Saclay, 91025, Evry-Courcouronnes, France.

[b] Department of Physics, University of Warwick, Gibbet Hill Road, Coventry CV4 7AL, United Kingdom

[c] Center for Interdisciplinary Research in Biology (CIRB), College de France, CNRS, INSERM, Université PSL, 75231 Paris, France

[d] CY Cergy Paris Université, Université d'Evry, Université Paris-Saclay, CNRS, LAMBE, F-95000, Cergy, France

[e] Institut Universitaire de France (IUF), 75231, Paris, France

* Corresponding author address: clement.campillo@univ-evry.fr

Abstract

The mechanical properties of living cells reflect their physiological and pathological state. In particular, cancer cells undergo cytoskeletal modifications that typically make them softer than healthy cells, a property that could be used as a diagnostic tool. However, this is challenging because cells are complex structures displaying a broad range of morphologies when cultured in standard 2D culture dishes. Here, we use adhesive micropatterns to impose the cell geometry and thus standardize the mechanics and morphologies of cancer cells, which we measure by atomic force microscopy (AFM) mechanical nanomapping and membrane nanotube pulling. We show that micropatterning cancer cells lead to distinct morphological and mechanical changes for different cell lines. Micropatterns did not systematically lower the variability in cell elastic modulus distribution. These effects emerge from a variable cell spreading rate associated with differences in the organization of the cytoskeleton, thus providing detailed insights into the structure-mechanics relationship of cancer cells cultured on micropatterns. Combining AFM with micropatterns reveals new mechanical and morphological observables applicable to cancer cells and possibly other cell types.

Keywords

Atomic force microscopy (AFM); Cell mechanics; Actin cytoskeleton; Micropatterning; Cancer

Introduction

The mechanical properties of cells affect many of their functions, such as motility or division [1,2]. Cells affected by disease can also change their mechanical properties: for instance, malaria-infected red blood cells become more rigid than healthy red blood cells[3], whereas individual cancer cells are generally softer than healthy cells[4–8]. Mechanical changes have also been measured at larger tissue scale: biopsies from invasive tumors are stiffer than benign ones [9]. Altogether, these results have stimulated dynamic research toward utilising mechanical measurements as a diagnostic tool[10,11].

However, comparing cell populations' mechanics to discriminate between pathological grades remains highly challenging because effective mechanical parameters, such as cell elasticity, display significant variability, both within single cells and between cells of the same population. This hampers the reliability of cell mechanics as biomarkers. Therefore, to further our understanding of cell mechanics and propose novel cancer biomarkers, the throughput, robustness, and precision of elasticity measurements must be improved. High throughput has been obtained by probing many cells using microfluidic experiments[12]. However, these experiments cannot provide measurements of local elasticity. Highlighting stiffness differences within cells requires nanometric probes such as those used in atomic force microscopy (AFM).

AFM is a powerful technique for studying the mechanics and morphology of living cancer cells[13–17] and extremely soft biomimetic materials[18]. The cell is generally treated as an isotropic, elastic material in AFM experiments. Controlled deformation applied over the whole cell with an AFM tip is used to measure an effective Young's modulus with a nanometric spatial resolution, providing maps of the cell's local elasticity, which often

correlates with the organization of the actin cytoskeleton[19–22]. Alternatively, using probes with a diameter in the order of micrometers leads to a more global measurement at the whole cell scale[23]. AFM also allows studying membrane nanotubes, cylinders of plasma membranes with a radius of a few tenths of nanometers formed from the cell surface. In these experiments, adhesive nanometric tips or cells attached to the AFM cantilever are first brought into contact with the cell surface and then retracted, inducing nanotube formation [24,25]. The force required to maintain a nanotube reflects the mechanical tension of the lipid membrane from which it is pulled and the attachment of this membrane to the underlying actin cortex[26,27].

To develop robust and high-throughput AFM mechanical mapping[28], it is necessary to standardize and parallelize the measurements to improve the amount of data and the statistical significance of potential differences between cancer cell populations. Substrates on which periodic adhesive micropatterns are printed allow growing cells with the same geometry, architecture, and microenvironment[29]. Therefore, it can reduce inter-and intra-cell variability in a sample and has been adapted for AFM experiments[30–32] and intracellular microrheology using optical tweezers[33].

Here, we use cancer cell lines representing different stages of breast cancer, from non-metastatic MCF7 to highly metastatic MDA-MB-231, to compare their morphological and mechanical parameters on or off micropatterns. We first use AFM to extract their surface, volume, and spreading ratio. Then, we map their elastic modulus and establish correlations between local elasticity, membrane nanotubes formation, actin cytoskeleton organization, and cell spreading rate to improve the characterization of cancer progression.

Results

Measuring cell topography and mechanics on micropatterned cancer cells.

Our experimental approach to probing the morphology and mechanics of cancer cells is presented in **Fig.1**. We acquire an optical bright-field image for each cell and then scan the cell using the QI™ Mode from JPK-Bruker (**Fig.1A**), providing a force-indentation curve

(**Fig.1B**) at each point of its surface. With our experimental parameters, we scan a single cell in 5 minutes. From the force-indentation curves, we first measure the height at which the tip touches the cell ("contact point"). We then calculate the local Young's modulus, hereafter named "elasticity" for simplicity, by fitting the approach curve with an elastic Sneddon model (see details in the Material & Methods section). We thus obtain a map of the cell topography and another for the cell mechanics. **Fig.1C,D, and E** exhibit these maps for an MDA-MB-231 cell adhered to a fibronectin-coated glass substrate without geometric constraints; this condition is hereafter named "free" cell; **Fig.1F,G, and H** for an MDA-MB-231 cell grown on a Y-shaped fibronectin micropattern, or "constrained" cell. Therefore, the substrate is identical in all our conditions; only the geometry of the cells changes. Note that we have tested various shapes and sizes of micropatterns and chosen this Y-shape as it gave the highest yield of individual patterned cells for all the cell lines that we investigated. In all our experiments, the indentation speed is 100 µm/s, and the force setpoint is 0.3 nN. Changing the speed or force setpoint by several orders of magnitude did not significantly affect our values of the cell elastic modulus and morphology (**Fig.S1**).

Next, we compare the morphology and mechanics of three types of breast cancer cells: non-invasive MCF-7, MCF-7 treated with Epidermal Growth Factor (EGF) to drive these cells across the Epithelial-Mesenchymal Transition[34,35] and highly invasive MDA-MB-231. We perform our AFM experiments on "constrained" or "free" cells yielding the six conditions we compare below.

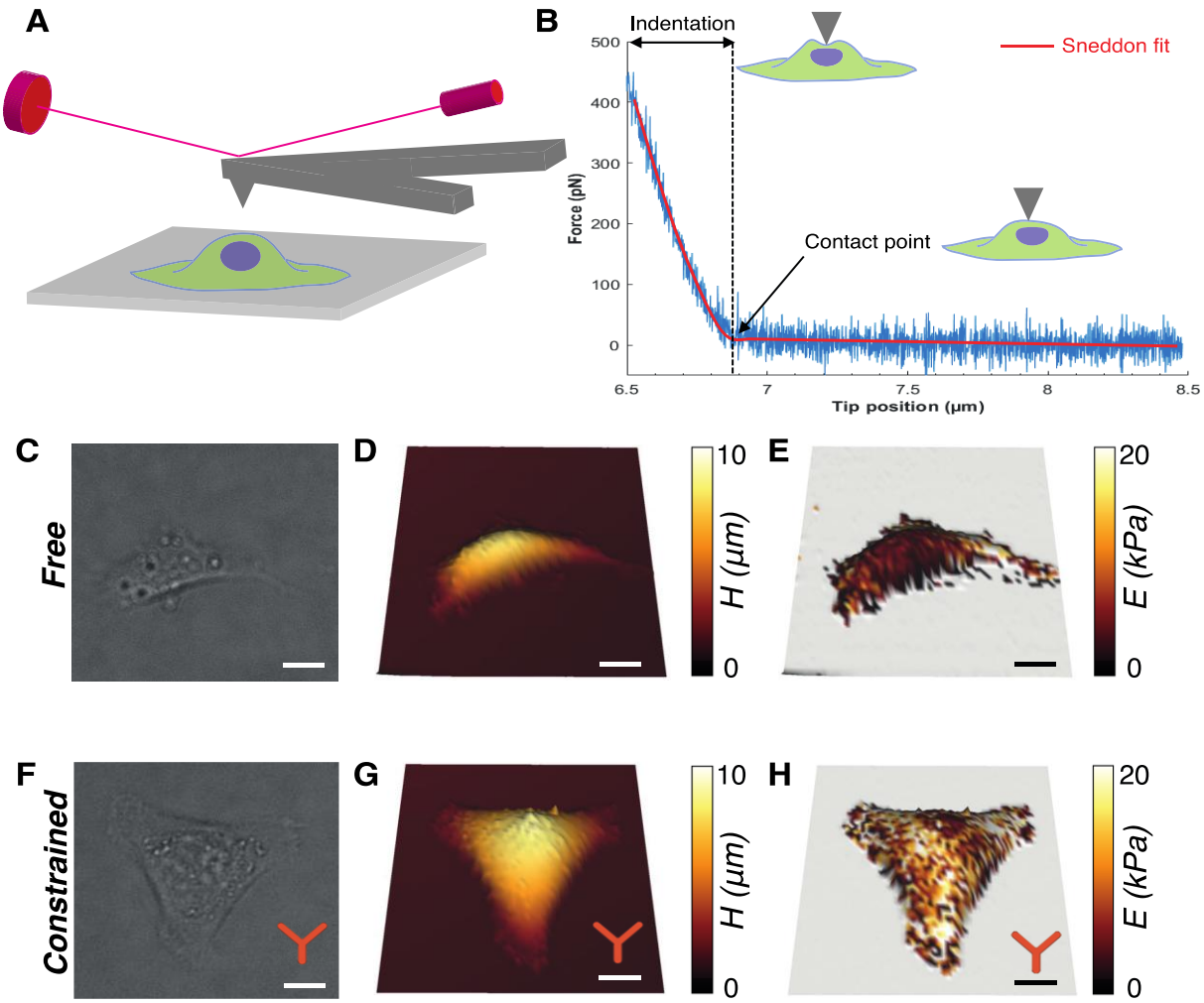

Figure 1. Nanomechanical mapping of adherent cancer cells. (**A**) Schematics of the AFM experiment. (**B**) Approach force curve (blue) fitted by a Sneddon model (red) to obtain the contact point and the local Young modulus, or elasticity, in the indentation region of the curve, indentation speed: 100 µm/s, force setpoint: 0.3 nN. (**C, F**) Optical bright field image showing an MDA-MB-231 cell spread on a fibronectin-coated plastic surface (C) and a Y-shaped fibronectin micropattern (F). (**D, G**) AFM height ($\overline{H}$) and (**E, H**) AFM elastic modulus ($\overline{E}$) maps of the cells shown in (C, F). Color codes depict the height of the contact point in (D, G) and the Young modulus in (E, H). Scale bars: 10 µm.

Cell morphology

First, we used AFM to assess the effect of patterning the cell substrate on the morphology of our cancer cells. From the AFM images, we extracted the cell total surface, defined as the

sum of the upper surface obtained by AFM and the lower projected surface (**Fig.2A**, see Materials and Methods) and the cell volume (**Fig.2B**). We then calculated their spreading ratio, a dimensionless parameter that measures how much the cell is spread on the substrate: it varies between 0 for a perfectly flat cell and 1 for a sphere (**Fig.2C**, see Materials and Methods).

Even if "free" cells have different spread areas, micropatterns imposed upon "constrained" cells a mean total surface of around 2500 μm^2 (2400 ± 300 and 2500 ± 400 μm^2 for MCF-7 and MDA-MB-231 cells, respectively, **Fig.2A**). On top of that, culturing cells on micropatterns significantly decreased the standard deviation of surfaces for all types of cells (from ± 1000 to ± 300 μm^2). On a standard fibronectin-coated glass substrate, MCF-7 cells had a larger mean volume than MDA-MB-231 cells (4200 ± 1200 vs. 3600 ± 1400 μm^3, respectively). When the cells are cultured on micropatterns, that difference in volume disappeared (**Fig.2B**). MCF-7 cells had a higher spreading ratio on the micropatterns than when they were unconstrained (0.34 ± 0.04 vs. 0.28 ± 0.06, respectively). In contrast, the spreading ratio of MDA-MB-231 cells was similar on both substrates. As a result, MCF-7 cells are less spread than MDA-MB231 cells on micropatterns (**Fig.2C**).

The addition of EGF to MCF-7 cells resulted in a significant increase in the mean surface for free (from 3000 ± 1000 to 4300 ± 1400 μm^2) and constrained cells (from 2400 ± 300 to 2600 ± 300 μm^2; see **Fig.2A**). EGF also induced a significant increase in mean volume for free (from 4200 ± 1200 to 5300 ± 1200 μm^3) and constrained cells (from 3900 ± 900 μm^3 to 4600 ± 1000 μm^3; see **Fig.2B**). EGF increases the spreading area and volume of the cells, but their spreading ratio remains constant (**Fig.2C**).

Therefore, for each cell line, the mean cell volume measured with or without geometrical constraint is similar, but the mean cell surface changes according to adhesion conditions; this effect determines the values of the spreading ratio (**Fig.2C**). Note that the cell surfaces and volumes we measured in this study are similar to those published elsewhere using AFM and confocal microscopy[36–38].

Using cell morphology measurements, we can build "average cells"[29,30] from the AFM images of the three types of constrained cells (**Fig.2D,E,F**, see Material & Methods for details). These maps confirm the results presented in **Fig.2A,B, and C**: MCF-7 cells have a larger volume than MDA-MB-231 cells; they also undergo a volume increase in the presence of EGF. These

results also provide a detailed view of the cell shape, as shown by the height profile measured at the top of the cell on these averaged maps (**Fig.2G**).

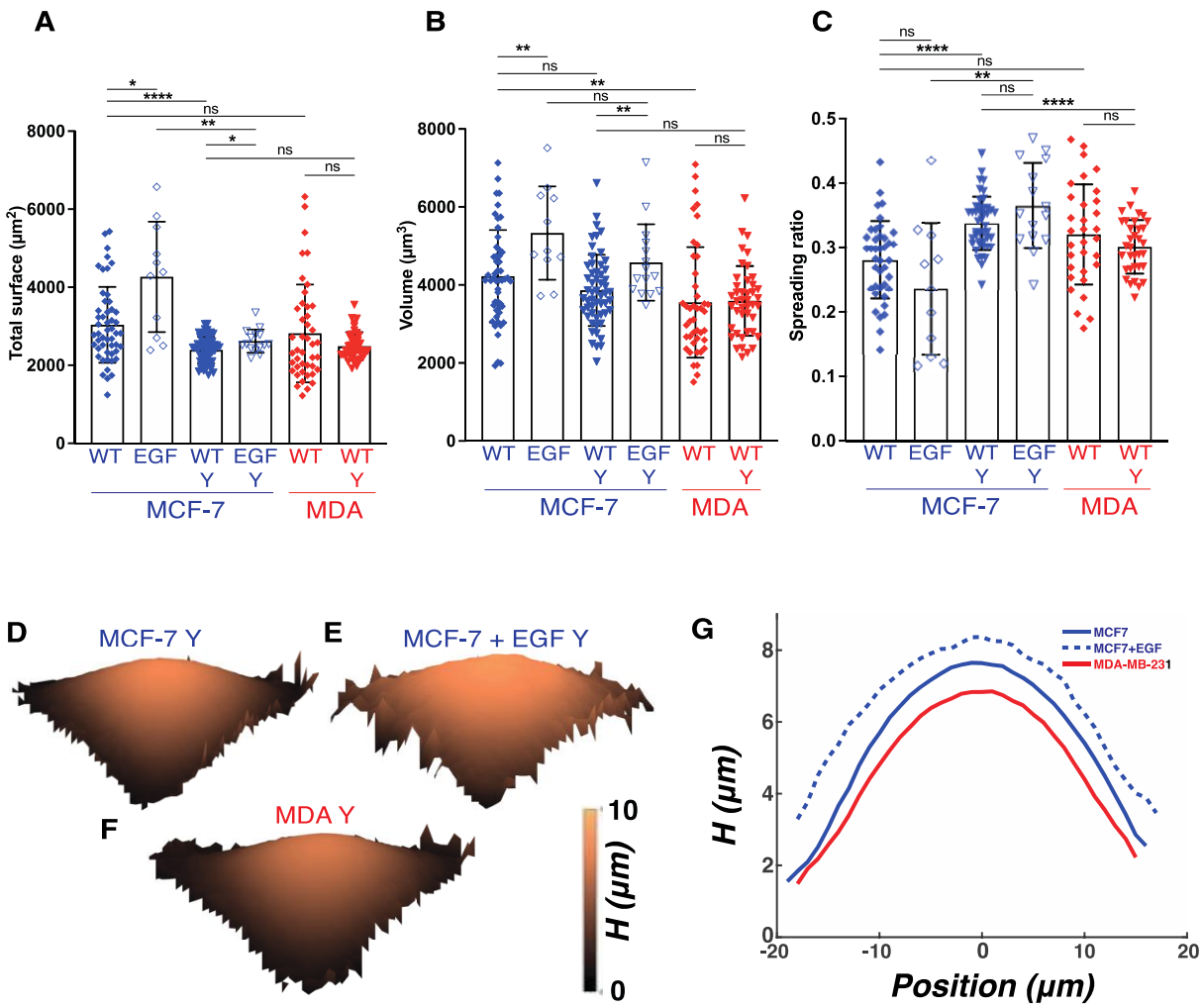

Figure 2: **Morphology of cancer cell lines extracted from AFM images**. **(A)** Surfaces, **(B)** Volumes, and **(C)** Spreading ratios. Each point corresponds to a single cell, MCF-7: N=51, MCF-7 + EGF: N=11, MCF-7 Y-pattern: N=55, MCF-7 Y-pattern + EGF : N=15, MDA : N= 43, MDA Y-pattern : N=43. Statistical analysis is performed using a Mann-Whitney test, ns $p > 0.05$; * $p \leq 0.05$; ** $p \leq 0.01$; *** $p \leq 0.001$; **** $p \leq 0.0001$. **(D,E,F)** Average topography of cells spread on Y-shaped fibronectin micropatterns. MCF-7: N-43, MCF-7 + EGF N=15 and MDA: N = 34. Scale bar: 10 µm. **(G)** Height profiles at the top of the cell for the average cells presented in (D,E,F).

Elasticity of micropatterned cancer cells

We use AFM elasticity maps to assess the role of micropatterning on the mechanics of our cancer cell lines. The cells' elastic modulus values can be presented in two complementary ways: averaging the elastic modulus cell by cell or averaging all the measurements obtained for a cell population. In **Fig.3A**, we show the geometric mean of the elastic modulus for each cell of our samples. We chose to use geometric means because elastic modulus distributions for a single cell are skewed **(Fig.S2)**, as already observed[39,40]. In **Fig.3B**, we present the distribution of all elastic modulus measurements we collected per condition (all cells combined, detailed measured elasticities in **Table S1**). We see that this method provides similar results to averaging cell by cell.

We observe that the effect of micropatterning the substrate on cell elastic modulus is markedly different depending on the cell type. As a control for cell elastic modulus measurements, we checked that unconstrained MCF-7 cells appeared stiffer than MDA-MB-231 cells (4.7 ± 2.1 vs 3.5 ± 2.0 kPa, respectively; see **Fig.3A**), which is in agreement with previous results reported by others[14,41]. Constraining MCF-7 cells had little effect on their elastic modulus (4.7 ± 2.1 vs 4.0 ± 1.5 kPa for free and constrained cells, respectively). Moreover, the effect of EGF on the elastic modulus of MCF-7 cells was barely noticeable for free cells (4.7 ± 2.1 vs 3.8 ± 1.7 kPa without EGF and with EGF, respectively); the effect was, however, prominent on micropatterns (4.0 ± 1.5 vs 1.3 ± 0.4 kPa without EGF and with EGF, respectively). Such decreases in elastic modulus related to increased aggressiveness of MCF7 cells triggered by the addition of EGF were previously observed[42]. For MDA-MB-231 cells, both the elastic modulus and its dispersion strongly increased when cells were constrained (3.5 ± 2.0 vs 7.3 ± 4.8 kPa for free and constrained cells, respectively), and they appeared stiffer than MCF-7 cells on micropattern, i.e., the difference in elastic modulus between these two cell lines was turned around from free to constrained cells. This difference was evidenced in the data where the elastic modulus is averaged cell-by-cell (**Fig.3A**) and the data where all elastic modulus measurements are pooled together (**Fig.3B**).

As a complementary experiment for force measurements collected with a nanoscale tip, we also tested our cells using a spherical probe with a much larger radius, in the order of micrometers, to obtain their elastic modulus at the scale of the whole cell (**Fig.2C**). We found

lower values of the cell elastic modulus with spherical probes compared to sharp tips, as already observed in several references[23,43,44]. This discrepancy between the two types of elasticity measurements has been attributed to differences in the contact area and indentation depth that could lead to probing different elements in the cells. Still, comparing our different conditions gave the same trends for both spherical probes and sharp tips. Importantly, we measured a higher and more dispersed elastic modulus in constrained MDA-MB-231 cells than in free MDA-MB-231 cells for the two types of experiments.

We then constructed average mechanical cells for the constrained conditions in the same manner as **Fig.2**. **Fig.3D,E,F** display 3D topographic representations of these average cells on which the elasticity maps have been superimposed (color-coded) to highlight the spatial distribution of cell stiffness. These panels with the same color code are in **Fig.S3.** They show, for instance, the effect of EGF, as the whole MCF-7 cell treated with EGF (**Fig.3E**) appears darker and is thus softer than the untreated cell (**Fig.3D**). Furthermore, the elastic modulus of the average MCF-7 cell is larger at the cell's periphery than in the middle of the cell; this effect is less noticeable in MCF-7 cells treated with EGF. The average MDA-MB-231 cell shows regions of higher elasticity, mainly at the extremities of the micropattern.

To further compare spatial elasticity distribution between our three patterned conditions, we separate elasticities into three groups corresponding to three regions: pattern tips, cell edges, and cell center, as depicted in **Fig.3G.** This allows us to plot the local elastic modulus as a function of the height while identifying the data points corresponding to these three regions **(Fig.3G,H,I)**. In all cases, higher elastic modulus values are located at the pattern extremities and cell edges, and the elastic modulus strongly increases with height in these regions. Oppositely, the elastic modulus in the center of the cell, which corresponds to measurements over three micrometers, is lower than at the cell periphery and does not depend on height for all conditions. We compare tips, edges, and centers for our three conditions in **Fig.3J**. We see that the values in the cell center correspond to the mean values presented in **Fig.3A**, with MDA cells appearing stiffer than MCF7 cells. This shows that the center of the cells largely contributes to the mean stiffness, mainly because this region provides most of the data points.

Finally, we studied the properties of membrane nanotubes formed from our various cell conditions (**Fig.3K**). In our experiments, we measure the force corresponding to the rupture

of a single nanotube, hereafter referred to as “nanotube force” (see **Fig.S4**). This force is determined by both membrane tension and membrane-cortex attachment[27]. We first showed that, for free cells, these forces are lower in MDA-MB-231 than in MCF7, as already observed [45]. This was particularly obvious for nanotubes formed from the lamellipodium of MDA-MB-231 cells, probably because the actin cytoskeleton is very dynamic in this region, and its connection with the membrane is weaker. We observed the opposite for patterned cells: tube forces are larger in MDA-MB-231 than in MCF7, especially at cell edges and centers. This mirrors the results obtained for cell elasticity (**Fig.3A,C).** We hypothesize that, as tube force is lower in the case of non-patterned MDA-MB-231 cells and that the membrane-cortex attachment has no reason to be modified by the micropatterning, this higher tube force for patterned cells could be the signature of a higher membrane tension [26,27] induced by the cell spreading on the micropatterns (see details further in the text).

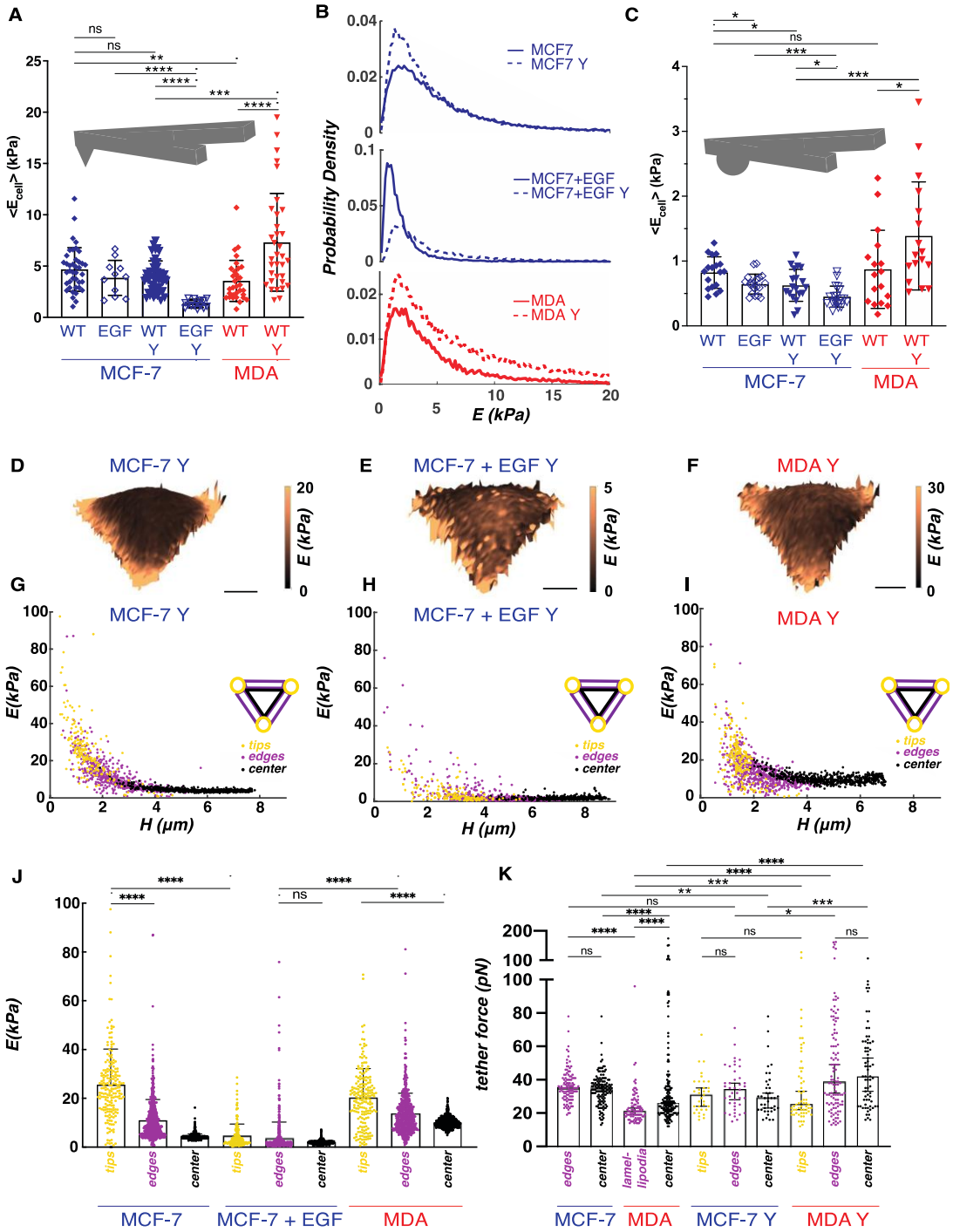

Figure 3: Elasticity of micropatterned cancer cells. (**A**) Mean elastic modulus of cancer cells measured from mechanical maps obtained with a sharp PF-QNM tip, patterned or not. Each point represents the geometric mean for a single cell. MCF-7: N=40, MCF-7 + EGF: N=11, MCF-7 Y-pattern: N=44, MCF-7 Y-pattern + EGF: N=15, MDA: N=32, MDA Y-pattern: N=34. Error bars depict the standard deviation of the different cells. Statistical analysis was performed using a Mann-Whitney test, ns $p > 0.05$; * $p \leq 0.05$; ** $p \leq 0.01$; *** $p \leq 0.001$; **** $p \leq 0.0001$. (**B**) Normalized histogram of all the elastic modulus measurements

performed on our six cell populations (**C**) Elastic modulus of cancer cells measured with a spherical probe. Each point represents the geometric mean for a single cell. MCF-7: N=18, MCF-7 + EGF: N=19, MCF-7 Y-pattern: N=19, MCF-7 Y-pattern + EGF: N=18, MDA: N=17, MDA Y-pattern: N=17. Same statistical analysis as in (A). (**D, E, F**) Average elastic modulus maps (color) overlaid on a 3D topographic representation of cells spread on Y-shaped micropatterns and local elastic modulus as a function of the cell height, obtained from respectively 43 MCF-7 (D), 15 MCF-7 + EGF (E), and 34 MDA (F). Scale bar: 10 µm. (**G, H, I**) Elastic modulus as a function of contact point height in pattern tips (yellow), edges (purple), and centers (black) for patterned MCF7, MCF+ EGF and MDA-MB-231 cells respectively **(J)** Elastic modulus distribution for average patterned cells in pattern tips, edges, and centers. Error bars depict the standard deviation. Statistical analysis was performed using a Mann-Whitney test, ns $p > 0.05$; * $p \leq 0.05$; ** $p \leq 0.01$; *** $p \leq 0.001$; **** $p \leq 0.0001$. All pairwise comparisons lead to p-values corresponding to *** or ****, except the ns shown in the figure. (**K**) Nanotube forces for various regions of free and patterned cancer cells. Bars display median values of the tube force and error bars 95% confidence interval. Statistical analysis was performed using a Mann-Whitney test, ns $p > 0.05$; * $p \leq 0.05$; ** $p \leq 0.01$; *** $p \leq 0.001$; **** $p \leq 0.0001$.

Cytoskeleton organization of micropatterned cancer cells

In this section, we test whether a strong correlation exists between the spatial distribution of cell stiffness and the intracellular organization of cells cultured on micropatterns. We fluorescently labelled the nucleus, microtubules, and actin filaments (F-actin) of cells cultured on micropatterns (**Fig.4A**). Microtubule organization and nuclear shape appeared similar in all cell lines (**Fig.S5**). On the other hand, F-actin was more concentrated at the cell periphery of MCF-7 cells, forming stress fibers between the Y branches[46]. A correlation with the elasticity map presented in **Fig.3D** can be observed: the areas of high elastic modulus correspond to those where the stress fibers were located. We used an algorithm to fit a spherical curve on the cell edges (**Fig.4B**) to measure the curvature radius R of the cell interface (**Fig.4C)**. This radius of curvature is proportional to the stress fibers' tension γ: $R = \gamma/\sigma$ [46,47], σ being the membrane tension. Hence, regions of high radius of curvature

correspond to high stress fiber tension and appear as stiff regions on elasticity maps[21]. We observe this for MCF-7 cells: they have the largest radii of curvature and hence the tightest actin stress cables, and elastic modulus is higher at their periphery. Conversely, MDA-MB-231 cells have less tensed boundaries, and we have shown that their elasticity was less polarized between the center and periphery. Moreover, using the measured values of R (168, 120, and 52 µm for MCF7, MCF7 + EGF, and MDA-MB-231, respectively) and a value of the membrane tension of $\sigma = 0.1$ mN/m[48], we obtained values of the stress fibers' tension of 17, 12 and 5 nN for MCF7, MCF7 + EGF and MDA-MB-231 respectively, in agreement with published values[46]. In MDA-MB-231 cells, F-actin appeared to accumulate at the extremities of the Y pattern and could correspond to focal adhesions[21]. Interestingly, the actin-rich regions, namely cell edges and pattern tips, also appeared stiffer on the elasticity maps for all our conditions (**Fig.3G**).

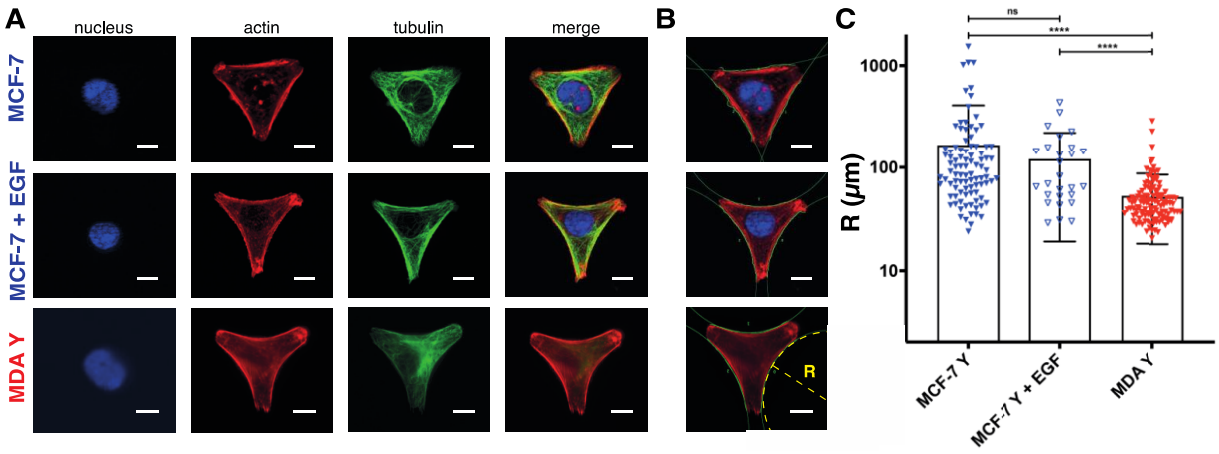

Figure 4: (A) Fluorescence images of typical MCF7, MCF7 +EGF, and MDA-MB-231 cells on Y-shaped micropatterns, labelled with DAPI, phalloidin-TRITC, and immunostaining of tubulin; (B) circles used to determine the radius of curvature R of the cell periphery. Scale bar: 10 µm. (C) Measurement of the curvature radius. Statistical analysis was performed using a t-test with Welch's correction; * $p \leq 0.2$; *** $p \leq 0.005$; **** $p \leq 0.0005$.

Correlation between spreading and elasticity

Finally, we investigated the relationship between two parameters: cell spreading ratio and elasticity. Since our AFM experiments provide maps of cell morphology and elasticity, we were able to simultaneously measure these two parameters for each cell. In **Fig.5,** we plot the average cell elastic modulus as a function of the cell spreading ratio. We observe a slight decrease in elastic modulus with the spreading ratio for free cells: the more the cells are spread, the stiffer they appear (**Fig.5A**). This trend is similar for all our conditions and was also observed in other studies[31]. On micropatterns, the range of accessible spreading ratios is limited for all cell types. MCF-7 cells, with or without EGF, do not show a sensitivity to the spreading ratio in this range: they are less spread out on patterns than when they are not constrained, and tiny variations of the spreading ratio do not affect their elasticity. The behaviour of MDA-MB-231 cells cultured on micropatterns is very different: the average value of the spreading ratio is close to that of unconstrained cells, but a small fraction of cells is strongly spread (spreading ratio < 0.3), and most of these appear highly stiff. These cells are the ones with very high elasticities observed in **Fig.3A**. Therefore, here, the intrinsic elasticity of the cell line is masked by the impact of the cell spreading on and off micropatterns. This agrees with the results of membrane nanotubes pulling experiments presented in **Fig.3K**. Rigato et al.[30] compared patterned and non-constrained non-cancerous RPE1 epithelial retinal cells. They showed that, considering the size of their micropatterns, free cells had a larger area than patterned cells, and were thus more spread, leading to a higher measured elasticity. This result is in very good agreement with our data showing a strong correlation between cell rigidity and cell spreading. Moreover, it shows that the relationship between spreading and elasticity is found beyond cancer cells. Besides, Mandal et al.[33] studied the difference between patterned cancer (MDA-MB-231) and non-cancer (MCF10A) breast cells and showed, studying intracellular rheology that the cancer cells were softer than the non-cancer ones on micropatterns, as it is the case in our experiments on free cells. Nevertheless, the spreading ratio of the cells is not easily accessible in these experiments, and thus it is hard to conclude on its effect on the measured mechanics. Moreover, they probe the interior of the cell, whereas we measure the elasticity of its surface, this could drastically change the relation between spreading and elasticity.

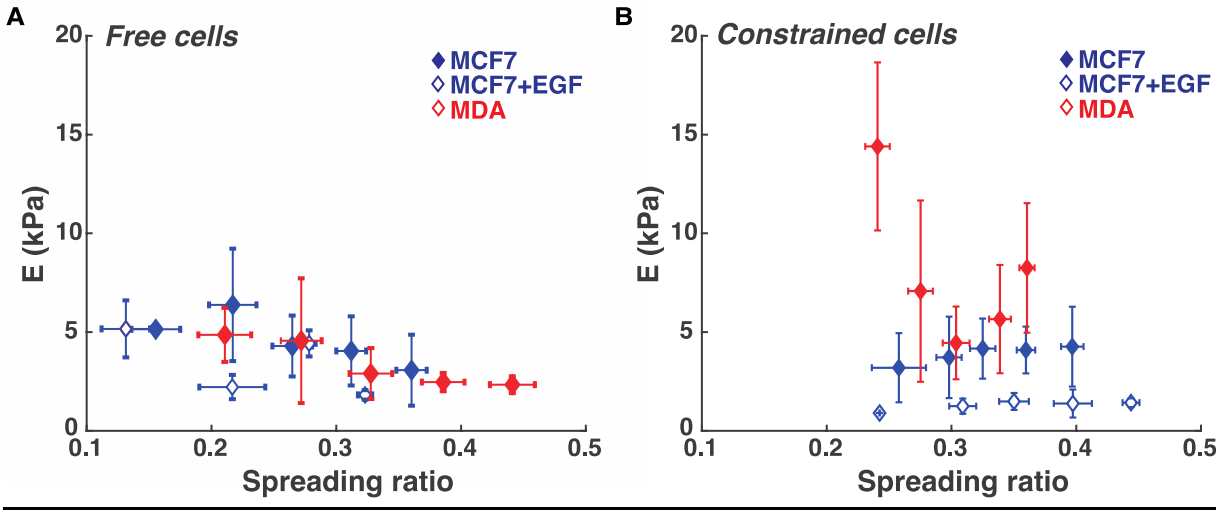

Figure 5: Relation between spreading ratio and average cell elastic modulus (A) for non-constrained cells (B) on Y-shaped micropatterns. Each point represents the mean value for 2 to 14 different cells, the total range of spreading ratio for each condition is cut into five parts of equivalent width, and all the cells falling in one part are averaged to obtain the point represented in the figure, error bars depict the standard deviation.

Conclusions

In this study, we characterized the elasticity and morphology of breast cancer cell lines reflecting cancer progression. Note that measuring the precise size of living cells is an experimental challenge[38]. We also imaged their actin cytoskeleton, whose spatial distribution correlates with the cells' morphology and elasticity. Unconstrained cells behave as expected: highly metastatic MDA-MB-231 cells appear softer than MCF7 cells. On micropatterns, the dispersion of MCF-7 cells' elastic modulus is lower than for free cells, and the cells are less spread, explaining why they appear softer. We have probed the cells both using nanomechanical mapping with sharp probes and using indentation with spherical probes: these two techniques provide similar trends in Young's modulus. Whereas nanomechanical mapping is useful to correlate the cell geometry with the elasticity

distribution, the latter approach is much faster to analyze many cells and obtain statistically significant differences between samples to discriminate cell populations[28].

MDA-MB-231 cell spreading is similar for unconstrained and micropatterned cells, but the elastic modulus and its dispersion are much larger than for MCF-7 cells. The elastic modulus vs spreading ratio curves (**Fig.5B**) indicate that a small fraction of the MDA-MB-231 cells spread very strongly on the patterns and appear very stiff, thus explaining why elastic modulus values are widely dispersed. Nanotube force measurements also support the hypothesis that MDA-MB-231 cells are under mechanical tension on micropatterns. One could hypothesize that the low fraction of highly spread MDA-MB-231 cells could be cancer stem cells (CSCs), that have indeed been identified in MDA-MB-231 cell lines[49]. In our experiments, we never observed any phenotypic alteration in the highly spread cells. To further determine if these cells are indeed CSCs, we would need to assess the presence of surface or intracellular markers such as CD44 or ALDH, respectively[50]. These experiments are beyond the scope of this article. Therefore, we cannot conclude on the nature of these highly-spread cells, but this will stimulate future experiments.

If some articles have investigated the effect of cell volume variations by osmotically deflating cells and measuring their stiffness[37,51], the spreading ratio, accessible only in AFM experiments combining stiffness and morphology mapping, thus seems to be an essential parameter to understand the biological source of the measured cell elasticity. As we show that the central region of the cell dominates the average cell elasticity, we hypothesize that our approach and in particular the spreading-mechanics relationship would be the same on micropatterns with different sizes and shapes. Besides, using micropatterns certainly forces structural changes on the cells before the measurement; therefore cells cannot be considered in their “natural” state. However, culturing cells on 2D surface does not reflect a “natural” setting either, even without the constraints induced by patterns, as cells exhibit a wide range of spreading behaviours that strongly affect their intrinsic elasticity[30].

Average elastic modulus and actin fluorescence maps reveal that MCF-7 cells only show regions of high stiffness at the cell periphery that colocalize with strong actin stress fibers. The measurement of the curvature of the cell interface confirms these results: MCF7 cells have stronger actin stress fibers and tighter interfaces. Conversely, MDA-MB-231 cells show

high stiffness mainly at the extremities of the patterns where actin-rich adhesive regions are located[46].

Finally, our patterning approach is beneficial to test the response of a single cell line to drugs, as we have clearly shown for MCF-7 cells treated or not with EGF. Our results show that many different cellular parameters are accessible using our approach: elasticity, surface, volume, cytoskeletal organization, curvature radius and tube force. In our experiments, most of these parameters taken alone can discriminate between cancerous cell lines such as MCF7 vs. MDA-MB-231. For diagnostic purposes, it would be useful first to adapt our approach to dissociated biopsies and then assess which mechanical and morphological parameters, or the most appropriate combination, correlate with the tumour grade. Such multivariate analysis has been done for stem cells[52] and cancer cells with another mechanical technique[53]. We thus believe our work has the potential to shape future research studies in which the morphological and mechanical properties of patient cells are exploited as novel diagnostic tools.

Materials and Methods

Cell culture

MCF7 are cultured in DMEM (Dulbecco's Modified Eagle's Medium, GIBCO) supplemented with 10% fetal bovine serum and 1% penicillin/streptomycin at 37°C with 5% CO2. MDA-MB-231 are cultured in Leibovitz's L-15 + GlutaMAX medium supplemented with 10% fetal bovine serum at 37°C. To drive them across the EMT, MCF7 are treated for 72h with 30 ng/mL EGF (Human Epidermal Growth Factor, EGF, Miltenyi Biotec #130-093-750). For AFM experiments on non-constrained cells, we coat Mattek Petri dishes (P35G-0-10-C) with fibronectin at the surface concentration of 5 µg/cm². Dishes are treated for 15 minutes with UV light and then incubated for one hour in a fibronectin solution in PBS. The dishes are then seeded with cells left to adhere for 12h. For cells adhered on fibronectin-coated micropatterns, we use the medium size Y-shaped patterns of CYTOO "Starter Chips" slides. The slide is fixed in a Petri dish and incubated for 30 min in a culture medium at 37°C. Then, the slides are seeded with 120000 cells, which are left to adhere for 12h.

Cell fluorescent labelling

We add a medium containing 5 µg/mL Hoechst (Hoechst 34580, BD Pharmingen #565877) for 1h to visualize the cell nuclei during AFM experiments. For immunofluorescence experiments, cells are fixed with formaldehyde at 3.7 % for 10 min and then rinsed twice with PBS. They are permeabilized with Triton X100 at 1% for 2 minutes, rinsed four times with PBS, and then incubated in 1% BSA solution for 30 minutes. We label DNA by incubating the cells for 4 min in a DAPI solution at 300 nM in PBS and then rinsing the cells four times with PBS. To label actin, we incubate the cells in a solution of phalloidin coupled to TRITC at one µg/mL in PBS for 30 min and then rinse the cells four times with PBS. To label tubulin, we incubated the cells in a solution of primary anti-β-tubulin monoclonal antibody (Sigma #T4026) diluted 200 times in PBS for two hours and then rinsed the cells four times in PBS. Then we incubated the cells in a solution of secondary polyclonal antibody coupled to Alexa Fluor 488 (Fisher Scientific #10256302) diluted 100 times in PBS for 1h30; finally, we rinsed the cells four times with PBS. We observe the cells with a 63 x /1.30 Plan-Neoflar objective on an ApoTome Axiovert 200 (Zeiss) microscope.

Atomic Force Microscopy

Measurements were performed using a Nanowizard 4 Bioscience AFM from JPK/Bruker placed on a vibration isolation table. We used the Quantitative Imaging™(QI) mode for nanomechanical mapping. In QI mode, the AFM tip is driven vertically downwards and upwards for each image pixel, thus collecting a force-distance curve at each approach-retract cycle. PeakForce QNM-Live Cell cantilevers (PFQNM-LC-A-CAL; Bruker AFM Probes) with a half opening angle of 15 °, a 17 µm high pyramidal tip, and a 65 nm tip radius were used. In our experiments, the indentation depth is 100 to 500 nm, always larger than the equivalent radius of the tip[54]. In all experiments, the sensitivity is first acquired by collecting a force curve on a stiff glass surface, and the cantilever's spring constant is obtained using the thermal tune method. The spring constant is in a range of 0.06 – 0.1 N/m. Force-indentation curves were collected with 100 µm/s probe velocity, 300 pN setpoint force, and 3 µm indentation-retraction distance over a variable area (1,500 – 10,000 μm^2, typically, the scanning area that is required to enclose an entire cell) with 64 × 64 pixels resolution. AFM

experiments are performed at room temperature in the culture medium of the cells, with 5% CO_2 in the case of MCF7. We used CP-CONT-PS-C cantilevers with a 6 µm radius spherical probe for larger-scale mechanical measurements. We measured their stiffness using a thermal tune method and obtained a typical value of 0.2 N/m. We indented the cells at a velocity of 2 µm/s and with a force setpoint of 5 nN. We record 15 indentation sequences per cell.

Analysis of force-displacement curves

Force-displacement curves are processed using the JPK Data Processing software (version 6.3.36). In all force curves, the piezo height is corrected with the cantilever deflection to get the accurate vertical tip position, which is then plotted as a function of the force. In the case of nanometric tips, the elastic modulus *E* is obtained by fitting a Sneddon model to the approach curves: $F = 0.8887 \frac{E}{1-\nu^2} tan\alpha\ \delta^2$, where F is the measured force, α the half opening angle of the tip, ν the Poisson ratio, assumed to be 0.5 for living cells, and δ the indentation. This analysis provides us with the contact point and Young's modulus for each image pixel. Then, we use a custom-built software tool coded in Matlab to treat these images. First, we correct the images for any bias in the flatness of the substrate; then, to collect elastic modulus values that correspond only to the cell (and not to the substrate), we apply thresholds to the images. We collect data corresponding to contact points over 100 nm over the substrate height, stiffness between 0 and 100 kPa, and local indentation of less than 30% of the cell height. The cell surface is the sum of the projected cell area plus the surface of the upper part, which is directly calculated from the contact points map: from the (x,y,z) positions of all contact points, we define triangles constituted by three adjacent contact points and then sum the areas of all these triangles in the region corresponding to the cell. To obtain the cell volume, we first multiply the contact point height by the area of a pixel, and then we sum all the individual volumes of each pixel of the image corresponding to a cell point. The cell spreading ratio is calculated as follows:

$$\frac{V}{\frac{4\pi}{3} \times \left(\sqrt{\frac{S}{4\pi}}\right)^3}$$

Where V is the cell volume in µm^3, and S is its surface in µm². This dimensionless quantity corresponds to the ratio of the cell volume over the volume of a sphere with the same area. υ tends toward 0 for the case of perfect wetting and to 1 for a sphere.

For cells cultured on micropatterns, we build average cells by determining the center of each cell, aligning the center of all the cells in each population, and finally calculating the average value of the contact point and stiffness in each point for all these cells.

For experiments in which cells are indented with micrometric beads, Young's modulus E is obtained by fitting a Hertz model to the approach curves: $F = \frac{E}{1-\nu^2}\frac{4\sqrt{R_C}}{3}\delta^{3/2}$, where F is the measured force, ν the Poisson ratio, still assumed to be 0.5, R_c the bead radius and δ the indentation.

Membrane nanotube-pulling experiments

For membrane tube pulling experiments, we use MLCT cantilevers from Bruker (k = 0.035 N/m) and coat the surface of the tips by immersing the tips in a solution of concanavalin A (Sigma) at 2.5 mg/mL in PBS for 15 min before the experiment. Then, the tip is positioned over the location of interest (either the centers, tips, or edges of the cells, see **Fig. 3**). For unconstrained cells, we measure only the centers and edges of MCF7 cells, as they display no visible tip, and only the centers and tips of MDA cells (the tips being analogous to lamellipodia in the case of MDA cells). We perform the tip approach at a speed of 5 µm/s until we reach a setpoint force of 200 pN. Contact between tip and cell is maintained for 1 s before retract curve is collected at 5 µm/s over a ramp length of 6 µm. Every event associated with the rupture of a membrane tube is characterized by a sudden jump in the force curve (see **Fig. S5**), and we record every force jump occurring further than 200 nm from the cell surface to filter out the effects due to specific or nonspecific adhesion of membrane proteins on the AFM tip. For each condition, we experiment over 4–9 cells and collect ~10 force curves for each location over a cell (tip, edge, or center).

Measurement of the radius of curvature:

To automatically measure the radius of curvature of Y-patterned cells, we developed a Fiji (Schindelin et al. 2012) plugin. The shape of each patterned cell was approximately an

isosceles triangle, and we detected each side of the triangle and measured its curvature. First, the contour of each cell was determined by classical thresholding of the actin channel: the “Intermodes” method was used, and when this method failed (no object above a given size was found), the “Triangle” method was called. Then, the 3 vertices of the triangle were determined by finding the 3 points with the maximum local density of points along the contour. For each side, or contour section in between two vertices, the contour was smoothed before fitting a circle using ImageJ’s Newton-based Pratt fit algorithm.

Supporting Information

Figure S1: Control experiments on the effect of AFM parameters on morphological and mechanical measurements.

Figure S2: Asymmetric elastic modulus distribution for individual cells

Table S3: Statistical parameters measured on the distribution of elastic modulus values for cell populations.

Figure S4: Average elastic modulus maps

Figure S5: Measurement of nanotube force in AFM experiments.

Figure S6: Nuclear morphology.

Acknowledgements

We acknowledge funding from the Université of Evry-Paris Saclay, the Genopole Biocluster at Evry, DIM Respore (Région Ile de France). Our group belongs to the CNRS consortium AQV.

Authors contributions

Maxime Liboz : Investigation, Validation, Formal Analysis ; Antoine Allard : Software ; Michel Malo: Resources, Conceptualisation ; Guillaume Lamour : Resources, Conceptualisation, Supervision, Writing ; Gaelle Letort: Software ; Bénédicte Thiébot : Resources, Conceptualisation ; Sid Labdi : Resources, Conceptualisation ; Juan Pelta : Resources, Conceptualisation ; Clément Campillo Conceptualisation, Supervision, Writing, Visualization, Project Administration

References

(1) Kunda, P.; Pelling, A. E.; Liu, T.; Baum, B. Moesin Controls Cortical Rigidity, Cell Rounding, and Spindle Morphogenesis during Mitosis. *Curr. Biol.* **2008**, *18* (2), 91–101. https://doi.org/10.1016/j.cub.2007.12.051.

(2) Chaigne, A.; Campillo, C.; Gov, N. S.; Voituriez, R.; Sykes, C.; Verlhac, M. H.; Terret, M. E. A Narrow Window of Cortical Tension Guides Asymmetric Spindle Positioning in the Mouse Oocyte. *Nat. Commun.* **2015**, *6*, 1–10. https://doi.org/10.1038/ncomms7027.

(3) Shelby, J. P.; White, J.; Ganesan, K.; Rathod, P. K.; Chiu, D. T. A Microfluidic Model for Single-Cell Capillary Obstruction by Plasmodium Falciparum- Infected Erythrocytes. *Proc. Natl. Acad. Sci. U. S. A.* **2003**, *100* (25), 14618–14622.

(4) Guck, J.; Schinkinger, S.; Lincoln, B.; Wottawah, F.; Ebert, S.; Romeyke, M.; Lenz, D.; Erickson, H. M.; Ananthakrishnan, R.; Mitchell, D.; Käs, J.; Ulvick, S.; Bilby, C. Optical Deformability as an Inherent Cell Marker for Testing Malignant Transformation and Metastatic Competence. *Biophys. J.* **2005**, *88*, 3689–3698.

(5) Alibert, C.; Goud, B.; Manneville, J. B. Are Cancer Cells Really Softer than Normal Cells? *Biol. Cell* **2017**, *109* (5), 167–189. https://doi.org/10.1111/boc.201600078.

(6) Smolyakov, G.; Thiebot, B.; Campillo, C.; Labdi, S.; Severac, C.; Pelta, J.; Dague, É. Elasticity, Adhesion, and Tether Extrusion on Breast Cancer Cells Provide a Signature of Their Invasive Potential. *ACS Appl. Mater. Interfaces* **2016**, *8* (41), 27426–27431. https://doi.org/10.1021/acsami.6b07698.

(7) Cross, S. E.; Jin, Y.-S.; Rao, J.; Gimzewski, J. K. Nanomechanical Analysis of Cells from Cancer Patients. *Nat. Nanotechnol.* **2007**, *2* (12), 780–783. https://doi.org/10.1038/nnano.2007.388.

(8) Fuhs, T.; Wetzel, F.; Fritsch, A. W.; Li, X.; Stange, R.; Pawlizak, S.; Kießling, T. R.; Morawetz, E.; Grosser, S.; Sauer, F.; Lippoldt, J.; Renner, F.; Friebe, S.; Zink, M.; Bendrat, K.; Braun, J.; Oktay, M. H.; Condeelis, J.; Briest, S.; Wolf, B.; Horn, L.-C.; Höckel, M.; Aktas, B.; Marchetti, M. C.; Manning, M. L.; Niendorf, A.; Bi, D.; Käs, J. A. Rigid Tumours Contain Soft Cancer Cells. *Nat. Phys.* **2022**, *18* (12), 1510–1519. https://doi.org/10.1038/s41567-022-01755-0.

(9) Plodinec, M.; Loparic, M.; Monnier, C. A.; Obermann, E. C.; Zanetti-dallenbach, R.;

Oertle, P.; Hyotyla, J. T.; Aebi, U.; Bentires-alj, M.; Lim, R. Y. H.; Schoenenberger, C. The Nanomechanical Signature of Breast Cancer. **2012**, *7* (November). https://doi.org/10.1038/nnano.2012.167.

(10) Guck, J. Some Thoughts on the Future of Cell Mechanics. *Biophysical Reviews*. 2019, pp 667–670. https://doi.org/10.1007/s12551-019-00597-0.

(11) Gensbittel, V.; Kräter, M.; Harlepp, S.; Busnelli, I.; Guck, J.; Goetz, J. G. Mechanical Adaptability of Tumor Cells in Metastasis. *Dev. Cell* **2021**, *56* (2), 164–179. https://doi.org/10.1016/j.devcel.2020.10.011.

(12) Otto, O.; Rosendahl, P.; Mietke, A.; Golfier, S.; Herold, C.; Klaue, D.; Girardo, S.; Pagliara, S.; Ekpenyong, A.; Jacobi, A.; Wobus, M.; Töpfner, N.; Keyser, U. F.; Mansfeld, J.; Fischer-Friedrich, E.; Guck, J. Real-Time Deformability Cytometry: On-the-Fly Cell Mechanical Phenotyping. *Nat. Methods* **2015**, *12* (3), 199–202. https://doi.org/10.1038/nmeth.3281.

(13) Vaziri, A.; Gopinath, A. Cell and Biomolecular Mechanics. *Nat. Mater.* **2008**, *7*, 15–23.

(14) Calzado-Martín, A.; Encinar, M.; Tamayo, J.; Calleja, M.; San Paulo, A. Effect of Actin Organization on the Stiffness of Living Breast Cancer Cells Revealed by Peak-Force Modulation Atomic Force Microscopy. *ACS Nano* **2016**, *10* (3), 3365–3374. https://doi.org/10.1021/acsnano.5b07162.

(15) Garcia, P. D.; Garcia, R. Determination of the Elastic Moduli of a Single Cell Cultured on a Rigid Support by Force Microscopy. *Biophys. J.* **2018**, *114* (12), 2923–2932. https://doi.org/10.1016/j.bpj.2018.05.012.

(16) Pelham, R. J.; Wang, Y.-L. Cell Locomotion and Focal Adhesions Are Regulated by Substrate Flexibility. *Proc. Natl. Acad. Sci. USA* **1997**, *94* (December), 13661–13665.

(17) Wang, H.; Zhang, H.; Da, B.; Lu, D.; Tamura, R.; Goto, K.; Watanabe, I.; Fujita, D.; Hanagata, N.; Kano, J.; Nakagawa, T.; Noguchi, M. Mechanomics Biomarker for Cancer Cells Unidentifiable through Morphology and Elastic Modulus. *Nano Lett.* **2021**, *21* (3), 1538–1545. https://doi.org/10.1021/acs.nanolett.1c00003.

(18) Lamour, G.; Allard, A.; Pelta, J.; Labdi, S.; Lenz, M.; Campillo, C. Mapping and Modeling the Nanomechanics of Bare and Protein-Coated Lipid Nanotubes. *Phys. Rev. X* **2020**, *10* (1), 11031. https://doi.org/10.1103/PhysRevX.10.011031.

(19) Rotsch, C.; Radmacher, M. Drug-Induced Changes of Cytoskeletal Structure and Mechanics in Fibroblasts: An Atomic Force Microscopy Study. *Biophys. J.* **2000**, *78* (1),

520–535. https://doi.org/10.1016/S0006-3495(00)76614-8.

(20) Eghiaian, F.; Rigato, A.; Scheuring, S. Structural, Mechanical, and Dynamical Variability of the Actin Cortex in Living Cells. *Biophys. J.* **2015**, *108* (6), 1330–1340. https://doi.org/10.1016/j.bpj.2015.01.016.

(21) Mandriota, N.; Friedsam, C.; Jones-Molina, J. A.; Tatem, K. V.; Ingber, D. E.; Sahin, O. Cellular Nanoscale Stiffness Patterns Governed by Intracellular Forces. *Nat. Mater.* **2019**, 1. https://doi.org/10.1038/s41563-019-0391-7.

(22) Abidine, Y.; Constantinescu, A.; Laurent, V. M.; Sundar Rajan, V.; Michel, R.; Laplaud, V.; Duperray, A.; Verdier, C. Mechanosensitivity of Cancer Cells in Contact with Soft Substrates Using AFM. *Biophys. J.* **2018**, *114* (5), 1165–1175. https://doi.org/10.1016/j.bpj.2018.01.005.

(23) Wu, P. H.; Aroush, D. R. Ben; Asnacios, A.; Chen, W. C.; Dokukin, M. E.; Doss, B. L.; Durand-Smet, P.; Ekpenyong, A.; Guck, J.; Guz, N. V.; Janmey, P. A.; Lee, J. S. H.; Moore, N. M.; Ott, A.; Poh, Y. C.; Ros, R.; Sander, M.; Sokolov, I.; Staunton, J. R.; Wang, N.; Whyte, G.; Wirtz, D. A Comparison of Methods to Assess Cell Mechanical Properties. *Nat. Methods* **2018**, *15* (7). https://doi.org/10.1038/s41592-018-0015-1.

(24) Krieg, M.; Helenius, J.; Heisenberg, C.; Muller, D. J. A Bond for a Lifetime : Employing Membrane Nanotubes from Living Cells to Determine Receptor – Ligand Kinetics. *Angew. Chemie Int Ed* **2008**, *47* (2), 9775–9777. https://doi.org/10.1002/anie.200803552.

(25) Puech, P.; Taubenberger, A.; Ulrich, F.; Krieg, M.; Muller, D. J.; Heisenberg, C. Measuring Cell Adhesion Forces of Primary Gastrulating Cells from Zebrafish Using Atomic Force Microscopy. *J. Cell Sci.* **2005**. https://doi.org/10.1242/jcs.02547.

(26) Dai, J.; Sheetz, M. P. Membrane Tether Formation from Blebbing Cells. *Biophys. J.* **1999**, *77*, 3363–3370.

(27) Sheetz, M. P. Cell Control by Membrane Cytoskeleton Adhesion. *Nat. Rev. Mol. Cell Biol.* **2001**, *2*, 392–396.

(28) Proa-Coronado, S.; Séverac, C.; Martinez-Rivas, A.; Dague, E. Beyond the Paradigm of Nanomechanical Measurements on Cells Using AFM: An Automated Methodology to Rapidly Analyse Thousands of Cells. *Nanoscale Horizons* **2020**, *5* (1), 131–138. https://doi.org/10.1039/c9nh00438f.

(29) Théry, M.; Racine, V.; Pépin, A.; Piel, M.; Chen, Y.; Sibarita, J.-B.; Bornens, M. The

Extracellular Matrix Guides the Orientation of the Cell Division Axis. *Nat. Cell Biol.* **2005**, *7* (10), 947–953. https://doi.org/10.1038/ncb1307.

(30) Rigato, A.; Rico, F.; Eghiaian, F.; Piel, M.; Scheuring, S. Atomic Force Microscopy Mechanical Mapping of Micropatterned Cells Shows Adhesion Geometry- Dependent Mechanical Response on Local and Global Scales. *ACS Nano* **2015**, *9* (6), 5846–5856. https://doi.org/10.1021/acsnano.5b00430.

(31) Roca-Cusachs, P.; Alcaraz, J.; Sunyer, R.; Samitier, J.; Farré, R.; Navajas, D. Micropatterning of Single Endothelial Cell Shape Reveals a Tight Coupling between Nuclear Volume in G1 and Proliferation. *Biophys. J.* **2008**, *94* (12), 4984–4995. https://doi.org/10.1529/biophysj.107.116863.

(32) Wang, X.; Hu, X.; Kawazoe, N.; Yang, Y.; Chen, G. Manipulating Cell Nanomechanics Using Micropatterns. *Adv. Funct. Mater.* **2016**, *26* (42), 7634–7643. https://doi.org/10.1002/adfm.201601585.

(33) Mandal, K.; Goud, B.; Manneville, J.-B. Mapping Intracellular Mechanics on Micropatterned Substrates. *Proc. Natl. Acad. Sci. U. S. A.* **2016**. https://doi.org/10.1073/pnas.1605112113.

(34) Kalluri, R.; Weinberg, R. A. The Basics of Epithelial-Mesenchymal Transition. *J. Clin. Invest.* **2009**, *119* (6), 1420–1428. https://doi.org/10.1172/JCI39104.

(35) Kim, J.; Kong, J.; Chang, H.; Kim, H.; Kim, A. EGF Induces Epithelial-Mesenchymal Transition through Phospho-Smad2/3-Snail Signaling Pathway in Breast Cancer Cells. *Oncotarget* **2016**, *7* (51), 85021–85032. https://doi.org/10.18632/oncotarget.13116.

(36) Xie, K.; Yang, Y.; Jiang, H. Controlling Cellular Volume via Mechanical and Physical Properties of Substrate. *Biophys. J.* **2018**, *114* (3), 675–687. https://doi.org/10.1016/j.bpj.2017.11.3785.

(37) Guo, M.; Pegoraro, A. F.; Mao, A.; Zhou, E. H.; Arany, P. R.; Han, Y.; Burnette, D. T.; Jensen, M. H.; Kasza, K. E.; Moore, J. R.; Mackintosh, F. C.; Fredberg, J. J.; Mooney, D. J.; Lippincott-Schwartz, J.; Weitz, D. A. Cell Volume Change through Water Efflux Impacts Cell Stiffness and Stem Cell Fate. *Proc. Natl. Acad. Sci.* **2017**, *114* (41), E8618 LP-E8627. https://doi.org/10.1073/pnas.1705179114.

(38) Cadart, C.; Venkova, L.; Piel, M.; Cosentino Lagomarsino, M. Volume Growth in Animal Cells Is Cell Cycle Dependent and Shows Additive Fluctuations. *Elife* **2022**, *11*, 1–18. https://doi.org/10.7554/eLife.70816.

(39) Limpert, E.; Stahel, W. A.; Abbt, M. Log-Normal Distributions across the Sciences: Keys and Clues: On the Charms of Statistics, and How Mechanical Models Resembling Gambling Machines Offer a Link to a Handy Way to Characterize Log-Normal Distributions, Which Can Provide Deeper Insight into V. *Bioscience* **2001**, *51* (5), 341–352. https://doi.org/10.1641/0006-3568(2001)051[0341:LNDATS]2.0.CO;2.

(40) Even, C.; Abramovici, G.; Delort, F.; Rigato, A. F.; Bailleux, V.; de Sousa Moreira, A.; Vicart, P.; Rico, F.; Batonnet-Pichon, S.; Briki, F. Mutation in the Core Structure of Desmin Intermediate Filaments Affects Myoblast Elasticity. *Biophys. J.* **2017**, *113* (3), 627–636. https://doi.org/10.1016/j.bpj.2017.06.020.

(41) Omidvar, R.; Tafazzoli-shadpour, M.; Ali, M. Atomic Force Microscope-Based Single Cell Force Spectroscopy of Breast Cancer Cell Lines : An Approach for Evaluating Cellular Invasion. *J. Biomech.* **2014**, *47* (13), 3373–3379. https://doi.org/10.1016/j.jbiomech.2014.08.002.

(42) Nikkhah, M.; Strobl, J. S.; Schmelz, E. M.; Agah, M. Evaluation of the Influence of Growth Medium Composition on Cell Elasticity. *J. Biomech.* **2011**, *44* (4), 762–766. https://doi.org/10.1016/j.jbiomech.2010.11.002.

(43) Rico, F.; Roca-Cusachs, P.; Gavara, N.; Farré, R.; Rotger, M.; Navajas, D. Probing Mechanical Properties of Living Cells by Atomic Force Microscopy with Blunted Pyramidal Cantilever Tips. *Phys. Rev. E - Stat. Nonlinear, Soft Matter Phys.* **2005**, *72* (2). https://doi.org/10.1103/PhysRevE.72.021914.

(44) Harris, A. R.; Charras, G. T. Experimental Validation of Atomic Force Microscopy-Based Cell Elasticity Measurements. *Nanotechnology* **2011**, *22* (34). https://doi.org/10.1088/0957-4484/22/34/345102.

(45) Smolyakov, G.; Thiebot, B.; Campillo, C.; Labdi, S.; Severac, C.; Pelta, J.; Dague, É. Elasticity, Adhesion, and Tether Extrusion on Breast Cancer Cells Provide a Signature of Their Invasive Potential. *ACS Appl. Mater. &Interfaces* **2016**, *8 (41)*, 27426–27431. https://doi.org/10.1021/acsami.6b07698.

(46) Théry, M.; Pépin, A.; Dressaire, E.; Chen, Y.; Bornens, M. Cell Distribution of Stress Fibres in Response to the Geometry of the Adhesive Environment. *Cell Motil. Cytoskeleton* **2006**, *63* (6), 341–355. https://doi.org/10.1002/cm.20126.

(47) Bar-ziv, R.; Tlusty, T.; Moses, E.; Safran, S. A.; Bershadsky, A. Pearling in Cells: A Clue to Understanding Cell Shape. *PNAS* **1999**, *96* (August), 10140–10145.

(48) Dai, J.; Sheetz, M. P.; Wan, X.; Morris, C. E. Membrane Tension in Swelling and Shrinking Molluscan Neurons. *J. Neurosci.* **1998**, *18* (17), 6681–6692. https://doi.org/10.1523/jneurosci.18-17-06681.1998.

(49) Hiraga, T.; Ito, S.; Nakamura, H. Side Population in MDA-MB-231 Human Breast Cancer Cells Exhibits Cancer Stem Cell-like Properties without Higher Bone-Metastatic Potential. *Oncol Rep* **2011**, *25* (1), 289–296. https://doi.org/10.3892/or_00001073.

(50) Walcher, L.; Kistenmacher, A. K.; Suo, H.; Kitte, R.; Dluczek, S.; Strauß, A.; Blaudszun, A. R.; Yevsa, T.; Fricke, S.; Kossatz-Boehlert, U. Cancer Stem Cells—Origins and Biomarkers: Perspectives for Targeted Personalized Therapies. *Front. Immunol.* **2020**, *11* (August), 1–33. https://doi.org/10.3389/fimmu.2020.01280.

(51) Zhou, E. H.; Trepat, X.; Park, C. Y.; Lenormand, G.; Oliver, M. N.; Mijailovich, S. M.; Hardin, C.; Weitz, D. A.; Butler, J. P.; Fredberg, J. J. Universal Behavior of the Osmotically Compressed Cell and Its Analogy to the Colloidal Glass Transition. *Proc. Natl. Acad. Sci. U. S. A.* **2009**, *106* (26), 10632–10637. https://doi.org/10.1073/pnas.0901462106.

(52) Lee, W. C.; Shi, H.; Poon, Z.; Nyan, L. M.; Kaushik, T.; Shivashankar, G. V.; Chan, J. K. Y.; Lim, C. T.; Han, J.; Van Vliet, K. J. Multivariate Biophysical Markers Predictive of Mesenchymal Stromal Cell Multipotency. *Proc. Natl. Acad. Sci. U. S. A.* **2014**, *111* (42), E4409–E4418. https://doi.org/10.1073/pnas.1402306111.

(53) Soteriou, D.; Kubánková, M.; Schweitzer, C.; López-Posadas, R.; Pradhan, R.; Thoma, O. M.; Györfi, A. H.; Matei, A. E.; Waldner, M.; Distler, J. H. W.; Scheuermann, S.; Langejürgen, J.; Eckstein, M.; Schneider-Stock, R.; Atreya, R.; Neurath, M. F.; Hartmann, A.; Guck, J. Rapid Single-Cell Physical Phenotyping of Mechanically Dissociated Tissue Biopsies. *Nat. Biomed. Eng.* **2023**. https://doi.org/10.1038/s41551-023-01015-3.

(54) Schillers, H.; Medalsy, I.; Hu, S.; Slade, A. L.; Shaw, J. E. PeakForce Tapping Resolves Individual Microvilli on Living Cells. *J. Mol. Recognit.* **2016**, *29* (2), 95–101. https://doi.org/10.1002/jmr.2510.

(1) Kunda, P.; Pelling, A. E.; Liu, T.; Baum, B. Moesin Controls Cortical Rigidity, Cell Rounding, and Spindle Morphogenesis during Mitosis. *Curr. Biol.* **2008**, *18* (2), 91–101. https://doi.org/10.1016/j.cub.2007.12.051.

(2) Chaigne, A.; Campillo, C.; Gov, N. S.; Voituriez, R.; Sykes, C.; Verlhac, M. H.; Terret, M. E. A Narrow Window of Cortical Tension Guides Asymmetric Spindle Positioning in the Mouse Oocyte. *Nat. Commun.* **2015**, *6*, 1–10. https://doi.org/10.1038/ncomms7027.

(3) Shelby, J. P.; White, J.; Ganesan, K.; Rathod, P. K.; Chiu, D. T. A Microfluidic Model for Single-Cell Capillary Obstruction by Plasmodium Falciparum- Infected Erythrocytes. *Proc. Natl. Acad. Sci. U. S. A.* **2003**, *100* (25), 14618–14622.

(4) Guck, J.; Schinkinger, S.; Lincoln, B.; Wottawah, F.; Ebert, S.; Romeyke, M.; Lenz, D.; Erickson, H. M.; Ananthakrishnan, R.; Mitchell, D.; Käs, J.; Ulvick, S.; Bilby, C. Optical Deformability as an Inherent Cell Marker for Testing Malignant Transformation and Metastatic Competence. *Biophys. J.* **2005**, *88*, 3689–3698.

(5) Alibert, C.; Goud, B.; Manneville, J. B. Are Cancer Cells Really Softer than Normal Cells? *Biol. Cell* **2017**, *109* (5), 167–189. https://doi.org/10.1111/boc.201600078.

(6) Smolyakov, G.; Thiebot, B.; Campillo, C.; Labdi, S.; Severac, C.; Pelta, J.; Dague, É. Elasticity, Adhesion, and Tether Extrusion on Breast Cancer Cells Provide a Signature of Their Invasive Potential. *ACS Appl. Mater. Interfaces* **2016**, *8* (41), 27426–27431. https://doi.org/10.1021/acsami.6b07698.

(7) Cross, S. E.; Jin, Y.-S.; Rao, J.; Gimzewski, J. K. Nanomechanical Analysis of Cells from Cancer Patients. *Nat. Nanotechnol.* **2007**, *2* (12), 780–783. https://doi.org/10.1038/nnano.2007.388.

(8) Fuhs, T.; Wetzel, F.; Fritsch, A. W.; Li, X.; Stange, R.; Pawlizak, S.; Kießling, T. R.; Morawetz, E.; Grosser, S.; Sauer, F.; Lippoldt, J.; Renner, F.; Friebe, S.; Zink, M.; Bendrat, K.; Braun, J.; Oktay, M. H.; Condeelis, J.; Briest, S.; Wolf, B.; Horn, L.-C.; Höckel, M.; Aktas, B.; Marchetti, M. C.; Manning, M. L.; Niendorf, A.; Bi, D.; Käs, J. A. Rigid Tumours Contain Soft Cancer Cells. *Nat. Phys.* **2022**, *18* (12), 1510–1519. https://doi.org/10.1038/s41567-022-01755-0.

(9) Plodinec, M.; Loparic, M.; Monnier, C. A.; Obermann, E. C.; Zanetti-dallenbach, R.; Oertle, P.; Hyotyla, J. T.; Aebi, U.; Bentires-alj, M.; Lim, R. Y. H.; Schoenenberger, C. The Nanomechanical Signature of Breast Cancer. **2012**, *7* (November). https://doi.org/10.1038/nnano.2012.167.

(10) Guck, J. Some Thoughts on the Future of Cell Mechanics. *Biophysical Reviews*. 2019, pp 667–670. https://doi.org/10.1007/s12551-019-00597-0.

(11) Gensbittel, V.; Kräter, M.; Harlepp, S.; Busnelli, I.; Guck, J.; Goetz, J. G. Mechanical Adaptability of Tumor Cells in Metastasis. *Dev. Cell* **2021**, *56* (2), 164–179. https://doi.org/10.1016/j.devcel.2020.10.011.

(12) Otto, O.; Rosendahl, P.; Mietke, A.; Golfier, S.; Herold, C.; Klaue, D.; Girardo, S.; Pagliara, S.; Ekpenyong, A.; Jacobi, A.; Wobus, M.; Töpfner, N.; Keyser, U. F.; Mansfeld, J.; Fischer-Friedrich, E.; Guck, J. Real-Time Deformability Cytometry: On-the-Fly Cell Mechanical Phenotyping. *Nat. Methods* **2015**, *12* (3), 199–202. https://doi.org/10.1038/nmeth.3281.

(13) Vaziri, A.; Gopinath, A. Cell and Biomolecular Mechanics. *Nat. Mater.* **2008**, *7*, 15–23.

(14) Calzado-Martín, A.; Encinar, M.; Tamayo, J.; Calleja, M.; San Paulo, A. Effect of Actin Organization on the Stiffness of Living Breast Cancer Cells Revealed by Peak-Force Modulation Atomic Force Microscopy. *ACS Nano* **2016**, *10* (3), 3365–3374. https://doi.org/10.1021/acsnano.5b07162.

(15) Garcia, P. D.; Garcia, R. Determination of the Elastic Moduli of a Single Cell Cultured on a Rigid Support by Force Microscopy. *Biophys. J.* **2018**, *114* (12), 2923–2932. https://doi.org/10.1016/j.bpj.2018.05.012.

(16) Pelham, R. J.; Wang, Y.-L. Cell Locomotion and Focal Adhesions Are Regulated by Substrate Flexibility. *Proc. Natl. Acad. Sci. USA* **1997**, *94* (December), 13661–13665.

(17) Wang, H.; Zhang, H.; Da, B.; Lu, D.; Tamura, R.; Goto, K.; Watanabe, I.; Fujita, D.; Hanagata, N.; Kano, J.; Nakagawa, T.; Noguchi, M. Mechanomics Biomarker for Cancer Cells Unidentifiable through Morphology and Elastic Modulus. *Nano Lett.* **2021**, *21* (3), 1538–1545. https://doi.org/10.1021/acs.nanolett.1c00003.

(18) Lamour, G.; Allard, A.; Pelta, J.; Labdi, S.; Lenz, M.; Campillo, C. Mapping and Modeling the Nanomechanics of Bare and Protein-Coated Lipid Nanotubes. *Phys. Rev. X* **2020**, *10* (1), 11031. https://doi.org/10.1103/PhysRevX.10.011031.

(19) Rotsch, C.; Radmacher, M. Drug-Induced Changes of Cytoskeletal Structure and

Mechanics in Fibroblasts: An Atomic Force Microscopy Study. *Biophys. J.* **2000**, *78* (1), 520–535. https://doi.org/10.1016/S0006-3495(00)76614-8.

(20) Eghiaian, F.; Rigato, A.; Scheuring, S. Structural, Mechanical, and Dynamical Variability of the Actin Cortex in Living Cells. *Biophys. J.* **2015**, *108* (6), 1330–1340. https://doi.org/10.1016/j.bpj.2015.01.016.

(21) Mandriota, N.; Friedsam, C.; Jones-Molina, J. A.; Tatem, K. V.; Ingber, D. E.; Sahin, O. Cellular Nanoscale Stiffness Patterns Governed by Intracellular Forces. *Nat. Mater.* **2019**, 1. https://doi.org/10.1038/s41563-019-0391-7.

(22) Abidine, Y.; Constantinescu, A.; Laurent, V. M.; Sundar Rajan, V.; Michel, R.; Laplaud, V.; Duperray, A.; Verdier, C. Mechanosensitivity of Cancer Cells in Contact with Soft Substrates Using AFM. *Biophys. J.* **2018**, *114* (5), 1165–1175. https://doi.org/10.1016/j.bpj.2018.01.005.

(23) Wu, P. H.; Aroush, D. R. Ben; Asnacios, A.; Chen, W. C.; Dokukin, M. E.; Doss, B. L.; Durand-Smet, P.; Ekpenyong, A.; Guck, J.; Guz, N. V.; Janmey, P. A.; Lee, J. S. H.; Moore, N. M.; Ott, A.; Poh, Y. C.; Ros, R.; Sander, M.; Sokolov, I.; Staunton, J. R.; Wang, N.; Whyte, G.; Wirtz, D. A Comparison of Methods to Assess Cell Mechanical Properties. *Nat. Methods* **2018**, *15* (7). https://doi.org/10.1038/s41592-018-0015-1.

(24) Krieg, M.; Helenius, J.; Heisenberg, C.; Muller, D. J. A Bond for a Lifetime : Employing Membrane Nanotubes from Living Cells to Determine Receptor – Ligand Kinetics. *Angew. Chemie Int Ed* **2008**, *47* (2), 9775–9777. https://doi.org/10.1002/anie.200803552.

(25) Puech, P.; Taubenberger, A.; Ulrich, F.; Krieg, M.; Muller, D. J.; Heisenberg, C. Measuring Cell Adhesion Forces of Primary Gastrulating Cells from Zebrafish Using Atomic Force Microscopy. *J. Cell Sci.* **2005**. https://doi.org/10.1242/jcs.02547.

(26) Dai, J.; Sheetz, M. P. Membrane Tether Formation from Blebbing Cells. *Biophys. J.* **1999**, *77*, 3363–3370.

(27) Sheetz, M. P. Cell Control by Membrane Cytoskeleton Adhesion. *Nat. Rev. Mol. Cell Biol.* **2001**, *2*, 392–396.

(28) Proa-Coronado, S.; Séverac, C.; Martinez-Rivas, A.; Dague, E. Beyond the Paradigm of Nanomechanical Measurements on Cells Using AFM: An Automated Methodology to Rapidly Analyse Thousands of Cells. *Nanoscale Horizons* **2020**, *5* (1), 131–138. https://doi.org/10.1039/c9nh00438f.

(29) Théry, M.; Racine, V.; Pépin, A.; Piel, M.; Chen, Y.; Sibarita, J.-B.; Bornens, M. The Extracellular Matrix Guides the Orientation of the Cell Division Axis. *Nat. Cell Biol.* **2005**, *7* (10), 947–953. https://doi.org/10.1038/ncb1307.

(30) Rigato, A.; Rico, F.; Eghiaian, F.; Piel, M.; Scheuring, S. Atomic Force Microscopy Mechanical Mapping of Micropatterned Cells Shows Adhesion Geometry- Dependent Mechanical Response on Local and Global Scales. *ACS Nano* **2015**, *9* (6), 5846–5856. https://doi.org/10.1021/acsnano.5b00430.

(31) Roca-Cusachs, P.; Alcaraz, J.; Sunyer, R.; Samitier, J.; Farré, R.; Navajas, D. Micropatterning of Single Endothelial Cell Shape Reveals a Tight Coupling between Nuclear Volume in G1 and Proliferation. *Biophys. J.* **2008**, *94* (12), 4984–4995. https://doi.org/10.1529/biophysj.107.116863.

(32) Wang, X.; Hu, X.; Kawazoe, N.; Yang, Y.; Chen, G. Manipulating Cell Nanomechanics Using Micropatterns. *Adv. Funct. Mater.* **2016**, *26* (42), 7634–7643. https://doi.org/10.1002/adfm.201601585.

(33) Mandal, K.; Goud, B.; Manneville, J.-B. Mapping Intracellular Mechanics on Micropatterned Substrates. *Proc. Natl. Acad. Sci. U. S. A.* **2016**. https://doi.org/10.1073/pnas.1605112113.

(34) Kalluri, R.; Weinberg, R. A. The Basics of Epithelial-Mesenchymal Transition. *J. Clin. Invest.* **2009**, *119* (6), 1420–1428. https://doi.org/10.1172/JCI39104.

(35) Kim, J.; Kong, J.; Chang, H.; Kim, H.; Kim, A. EGF Induces Epithelial-Mesenchymal Transition through Phospho-Smad2/3-Snail Signaling Pathway in Breast Cancer Cells. *Oncotarget* **2016**, *7* (51), 85021–85032. https://doi.org/10.18632/oncotarget.13116.

(36) Xie, K.; Yang, Y.; Jiang, H. Controlling Cellular Volume via Mechanical and Physical Properties of Substrate. *Biophys. J.* **2018**, *114* (3), 675–687. https://doi.org/10.1016/j.bpj.2017.11.3785.

(37) Guo, M.; Pegoraro, A. F.; Mao, A.; Zhou, E. H.; Arany, P. R.; Han, Y.; Burnette, D. T.; Jensen, M. H.; Kasza, K. E.; Moore, J. R.; Mackintosh, F. C.; Fredberg, J. J.; Mooney, D. J.; Lippincott-Schwartz, J.; Weitz, D. A. Cell Volume Change through Water Efflux Impacts Cell Stiffness and Stem Cell Fate. *Proc. Natl. Acad. Sci.* **2017**, *114* (41), E8618 LP-E8627. https://doi.org/10.1073/pnas.1705179114.

(38) Cadart, C.; Venkova, L.; Piel, M.; Cosentino Lagomarsino, M. Volume Growth in Animal Cells Is Cell Cycle Dependent and Shows Additive Fluctuations. *Elife* **2022**, *11*, 1–18. https://doi.org/10.7554/eLife.70816.

(39) Limpert, E.; Stahel, W. A.; Abbt, M. Log-Normal Distributions across the Sciences: Keys and Clues: On the Charms of Statistics, and How Mechanical Models Resembling Gambling Machines Offer a Link to a Handy Way to Characterize Log-Normal Distributions, Which Can Provide Deeper Insight into V. *Bioscience* **2001**, *51* (5), 341–352. https://doi.org/10.1641/0006-3568(2001)051[0341:LNDATS]2.0.CO;2.

(40) Even, C.; Abramovici, G.; Delort, F.; Rigato, A. F.; Bailleux, V.; de Sousa Moreira, A.; Vicart, P.; Rico, F.; Batonnet-Pichon, S.; Briki, F. Mutation in the Core Structure of Desmin Intermediate Filaments Affects Myoblast Elasticity. *Biophys. J.* **2017**, *113* (3), 627–636. https://doi.org/10.1016/j.bpj.2017.06.020.

(41) Omidvar, R.; Tafazzoli-shadpour, M.; Ali, M. Atomic Force Microscope-Based Single Cell Force Spectroscopy of Breast Cancer Cell Lines : An Approach for Evaluating Cellular Invasion. *J. Biomech.* **2014**, *47* (13), 3373–3379. https://doi.org/10.1016/j.jbiomech.2014.08.002.

(42) Nikkhah, M.; Strobl, J. S.; Schmelz, E. M.; Agah, M. Evaluation of the Influence of Growth Medium Composition on Cell Elasticity. *J. Biomech.* **2011**, *44* (4), 762–766. https://doi.org/10.1016/j.jbiomech.2010.11.002.

(43) Rico, F.; Roca-Cusachs, P.; Gavara, N.; Farré, R.; Rotger, M.; Navajas, D. Probing Mechanical Properties of Living Cells by Atomic Force Microscopy with Blunted Pyramidal Cantilever Tips. *Phys. Rev. E - Stat. Nonlinear, Soft Matter Phys.* **2005**, *72* (2). https://doi.org/10.1103/PhysRevE.72.021914.

(44) Harris, A. R.; Charras, G. T. Experimental Validation of Atomic Force Microscopy-Based

Cell Elasticity Measurements. *Nanotechnology* **2011**, *22* (34). https://doi.org/10.1088/0957-4484/22/34/345102.

(45) Smolyakov, G.; Thiebot, B.; Campillo, C.; Labdi, S.; Severac, C.; Pelta, J.; Dague, É. Elasticity, Adhesion, and Tether Extrusion on Breast Cancer Cells Provide a Signature of Their Invasive Potential. *ACS Appl. Mater. &Interfaces* **2016**, *8 (41)*, 27426–27431. https://doi.org/10.1021/acsami.6b07698.

(46) Théry, M.; Pépin, A.; Dressaire, E.; Chen, Y.; Bornens, M. Cell Distribution of Stress Fibres in Response to the Geometry of the Adhesive Environment. *Cell Motil. Cytoskeleton* **2006**, *63* (6), 341–355. https://doi.org/10.1002/cm.20126.

(47) Bar-ziv, R.; Tlusty, T.; Moses, E.; Safran, S. A.; Bershadsky, A. Pearling in Cells: A Clue to Understanding Cell Shape. *PNAS* **1999**, *96* (August), 10140–10145.

(48) Dai, J.; Sheetz, M. P.; Wan, X.; Morris, C. E. Membrane Tension in Swelling and Shrinking Molluscan Neurons. *J. Neurosci.* **1998**, *18* (17), 6681–6692. https://doi.org/10.1523/jneurosci.18-17-06681.1998.

(49) Hiraga, T.; Ito, S.; Nakamura, H. Side Population in MDA-MB-231 Human Breast Cancer Cells Exhibits Cancer Stem Cell-like Properties without Higher Bone-Metastatic Potential. *Oncol Rep* **2011**, *25* (1), 289–296. https://doi.org/10.3892/or_00001073.

(50) Walcher, L.; Kistenmacher, A. K.; Suo, H.; Kitte, R.; Dluczek, S.; Strauß, A.; Blaudszun, A. R.; Yevsa, T.; Fricke, S.; Kossatz-Boehlert, U. Cancer Stem Cells—Origins and Biomarkers: Perspectives for Targeted Personalized Therapies. *Front. Immunol.* **2020**, *11* (August), 1–33. https://doi.org/10.3389/fimmu.2020.01280.

(51) Zhou, E. H.; Trepat, X.; Park, C. Y.; Lenormand, G.; Oliver, M. N.; Mijailovich, S. M.; Hardin, C.; Weitz, D. A.; Butler, J. P.; Fredberg, J. J. Universal Behavior of the Osmotically Compressed Cell and Its Analogy to the Colloidal Glass Transition. *Proc. Natl. Acad. Sci. U. S. A.* **2009**, *106* (26), 10632–10637. https://doi.org/10.1073/pnas.0901462106.

(52) Lee, W. C.; Shi, H.; Poon, Z.; Nyan, L. M.; Kaushik, T.; Shivashankar, G. V.; Chan, J. K. Y.; Lim, C. T.; Han, J.; Van Vliet, K. J. Multivariate Biophysical Markers Predictive of Mesenchymal Stromal Cell Multipotency. *Proc. Natl. Acad. Sci. U. S. A.* **2014**, *111* (42),

E4409–E4418. https://doi.org/10.1073/pnas.1402306111.

(53) Soteriou, D.; Kubánková, M.; Schweitzer, C.; López-Posadas, R.; Pradhan, R.; Thoma, O. M.; Györfi, A. H.; Matei, A. E.; Waldner, M.; Distler, J. H. W.; Scheuermann, S.; Langejürgen, J.; Eckstein, M.; Schneider-Stock, R.; Atreya, R.; Neurath, M. F.; Hartmann, A.; Guck, J. Rapid Single-Cell Physical Phenotyping of Mechanically Dissociated Tissue Biopsies. *Nat. Biomed. Eng.* **2023**. https://doi.org/10.1038/s41551-023-01015-3.

(54) Schillers, H.; Medalsy, I.; Hu, S.; Slade, A. L.; Shaw, J. E. PeakForce Tapping Resolves Individual Microvilli on Living Cells. *J. Mol. Recognit.* **2016**, *29* (2), 95–101. https://doi.org/10.1002/jmr.2510.